Metabolic Engineering Communications 18 (2024) e00239

Contents lists available at ScienceDirect

Metabolic Engineering Communications

journal homepage: www.elsevier.com/locate/mec

^{13}C-metabolic flux analysis reveals metabolic rewiring in HL-60 neutrophil-like cells through differentiation and immune stimulation

Takeo Taniguchi [a], Nobuyuki Okahashi [a,b,c,*], Fumio Matsuda [a,b,c]

[a] Department of Bioinformatic Engineering, Graduate School of Information Science and Technology, Osaka University, 1-5 Yamadaoka, Suita, Osaka 565-0871, Japan
[b] Department of Biotechnology, Osaka University Shimadzu Analytical Innovation Research Laboratory, Graduate School of Engineering, Osaka University, 2-1 Yamadaoka, Suita, Osaka 565-0871, Japan
[c] Industrial Biotechnology Initiative Division, Institute for Open and Transdisciplinary Research Initiatives, Osaka University, 2-1 Yamadaoka, Suita, Osaka 565-0871, Japan

ARTICLE INFO

Keywords:
^{13}C-metabolic flux analysis
Neutrophil
HL-60
Differentiation
Immune response

ABSTRACT

Neutrophils are innate immune cells and the first line of defense for the maintenance of homeostasis. However, our knowledge of the metabolic rewiring associated with their differentiation and immune stimulation is limited. Here, quantitative ^{13}C-metabolic flux analysis was performed using HL-60 cells as the neutrophil model. A metabolic model for ^{13}C-metabolic flux analysis of neutrophils was developed based on the accumulation of ^{13}C in intracellular metabolites derived from ^{13}C-labeled extracellular carbon sources and intracellular macromolecules. Aspartate and glutamate in the medium were identified as carbon sources that enter central carbon metabolism. Furthermore, the breakdown of macromolecules, estimated to be fatty acids and nucleic acids, was observed. Based on these results, a modified metabolic model was used for ^{13}C-metabolic flux analysis of undifferentiated, differentiated, and lipopolysaccharide (LPS)-activated HL-60 cells. The glucose uptake rate and glycolytic flux decreased with differentiation, whereas the tricarboxylic acid (TCA) cycle flux remained constant. The addition of LPS to differentiated HL-60 cells activated the glucose uptake rate and pentose phosphate pathway (PPP) flux levels, resulting in an increased rate of total NADPH regeneration, which could be used to generate reactive oxygen species. The flux levels of fatty acid degradation and synthesis were also increased in LPS-activated HL-60 cells. Overall, this study highlights the quantitative metabolic alterations in multiple pathways via the differentiation and activation of HL-60 cells using ^{13}C-metabolic flux analysis.

1. Introduction

Neutrophils are a type of leukocytes that differentiate from myeloid progenitor cells and account for more than half of human leukocytes. Neutrophils play a crucial role in innate immunity by maintaining whole-body homeostasis. Notably, neutrophils produce reactive oxygen species (ROS) via NADPH oxidase to kill phagocytosed pathogens (Burn et al., 2021; Nauseef and Borregaard, 2014; Winterbourn et al., 2016), suggesting a close relationship between neutrophil metabolism and differentiation/function.

Differentiation-associated metabolic shifts occur in various cell types and are often described as a switching model between glycolysis- or oxidative phosphorylation (OXPHOS)-dominant modes. Compared to progenitor cells, differentiated osteoblasts and neurons prefer glycolysis and OXPHOS, respectively (Agostini et al., 2016; Guntur et al., 2018). For immune cells, naïve T cells rewire their glycolysis metabolism to OXPHOS via differentiation from their progenitor cells (Buck et al., 2015). Specific metabolic pathways associated with differentiation have also been found for neutrophils, in which fatty acid oxidation and glycogen accumulation are necessary during their differentiation (Kumar and Dikshit, 2019; Riffelmacher et al., 2017). Mature neutrophils have been reported to shift their metabolism from glycolysis to OXPHOS for energy production (Jeon et al., 2020). However, whether the metabolic rewiring of neutrophil differentiation follows the switching model of glycolysis and OXPHOS, similar to other cell types, is unclear as metabolic alterations before and after differentiation have not been quantitatively evaluated.

According to recent studies, metabolic rewiring in immune cells is

* Corresponding author. Department of Bioinformatic Engineering, Graduate School of Information Science and Technology, Osaka University, 1-5 Yamadaoka, Suita, Osaka 565-0871, Japan.
E-mail addresses: takeo_taniguchi@ist.osaka-u.ac.jp (T. Taniguchi), n-okahashi@ist.osaka-u.ac.jp (N. Okahashi), fmatsuda@ist.osaka-u.ac.jp (F. Matsuda).

https://doi.org/10.1016/j.mec.2024.e00239
Received 19 January 2024; Received in revised form 23 May 2024; Accepted 24 May 2024
Available online 27 May 2024

associated with cellular immune functions (O'Neill et al., 2016). Neutrophil metabolism is also closely related with their function, as its importance has long been revealed (Ardati et al., 1997; Borregaard and Herlin, 1982; Jeon et al., 2020; Loftus and Finlay, 2016); this is because ROS are produced from NADPH regenerated in central carbon metabolism. The capacity of neutrophils for pathogen clearance is compromised by the inhibition of lactate dehydrogenase via sodium oxamate and glucose-deficient culture (Awasthi et al., 2019; Rodríguez-Espinosa et al., 2015). A remarkable increase in the PPP flux by phorbol myristate acetate (PMA) stimulation has also been reported (Britt et al., 2022). However, quantitative knowledge of the metabolic shift coupled with immune activation in central carbon metabolism, including the TCA cycle, is lacking. Generally, neutrophils have fewer mitochondria than other immune cells that engage in acquired immunity (Kominsky et al., 2010). However, neutrophil mitochondria are also required for apoptosis and neutrophil extracellular trap formation (Maianski et al., 2003; Raam et al., 2008; Remijsen et al., 2011). Glutamine and fatty acids that fuel the TCA cycle are crucial for neutrophil function (Curi et al., 2020), implying the importance of mitochondrial activity in neutrophils. These carbon sources can drive NADPH-regenerating enzymes, such as isocitrate dehydrogenase (IDH) and malic enzyme (ME), to participate in neutrophil functions.

^{13}C-metabolic flux analysis is a promising solution for revealing quantitative metabolic shifts via differentiation and immune responses in neutrophils. This analysis allows the quantification of intracellular metabolic flux distribution by minimizing the residual sum of squares (RSS) of the measured and simulated influx of carbon sources, efflux of secreted products, and ^{13}C-labeling of intracellular metabolites using an *in silico* metabolic model. This technique was originally developed for the analysis of microbial cells and has been extended to elucidate the metabolism of mammalian cells, such as CHO cells, cancer cells, and hemocytes (Antoniewicz, 2018; Crown and Antoniewicz, 2013; Metallo et al., 2009; Sake et al., 2022; Stephanopoulos, 1999). To expand the use of this technology to these new subjects, first, the metabolic model must be evaluated (Moiz et al., 2023); such efforts have led to the discovery of new metabolic pathways (Amador-Noguez et al., 2010; Jiang et al., 2017; Leighty and Antoniewicz, 2012; Moiz et al., 2021; Okahashi et al., 2017).

In this study, we quantitatively characterized the metabolic rewiring of undifferentiated, differentiated, and LPS-activated HL-60 cells, an authentic model of human neutrophils (Breitman et al., 1980), using ^{13}C-metabolic flux analysis. The metabolic model used for ^{13}C-metabolic flux analysis was investigated by culturing HL-60 cells in media in which various carbon sources were replaced individually with uniformly ^{13}C-labeled carbon sources. The metabolic flux distributions of the three cell types, calculated via ^{13}C-metabolic flux analysis, provided insights into the shift in central carbon metabolism and cofactor regeneration through differentiation and immune responses.

2. Materials and methods

2.1. Cell line and culture

HL-60 human leukemia cells were obtained from the Japanese Collection of Research Bioresources (JCRB) Cell Bank (Osaka, Japan). Cells were cultured in a humidified atmosphere of 5% CO_2 at 37 °C, and maintained in Roswell Park Memorial Institute (RPMI) 1640 medium (Fujifilm Wako Pure Chemical Corporation, Osaka, Japan) supplemented with 10% heat-inactivated fetal bovine serum (FBS, Life Technologies, Carlsbad, CA, USA) and 1% penicillin/streptomycin (Fujifilm Wako Pure Chemical Corporation). HL-60 cells were differentiated into neutrophil-like cells via the addition of 1 μM retinoic acid (Sigma-Aldrich, St. Louis, MO, USA) followed by culture for 6 days. The cells were also stimulated with 10 μg/mL of LPS from *E. coli* O111:B4 (Sigma-Aldrich). For ^{13}C-metabolic flux analysis, 3.0×10^6 undifferentiated and 2.4×10^5 differentiated, and LPS-activated HL-60 cells were cultured in 5 mL of RPMI 1640 without glucose and sodium bicarbonate (Sigma-Aldrich) but supplemented with 5 mM [1,2–$^{13}C_2$]glucose (Cambridge Isotope Laboratories, Andover, MA, USA; >99% purity), 2.0 g/L sodium bicarbonate, and 10% dialyzed FBS (Life Technologies) for 48 h in 60-mm plates. Other ^{13}C-tracing experiments were performed under the same conditions using RPMI 1640 with a corresponding carbon source replaced by [U–$^{13}C_6$]glucose, [U–$^{13}C_5$]glutamine, [U–$^{13}C_5$]arginine, [U–$^{13}C_5$]glutamic acid, [U–$^{13}C_4$]aspartic acid, [U–$^{13}C_3$]serine, [U–$^{13}C_5$] proline, or [U–$^{13}C_6$]leucine (Cambridge Isotope Laboratories, >99% purity). Owing to rapid glucose consumption, the glucose concentration was increased to 10 mM for undifferentiated HL-60 cells. Viable cells were counted using trypan blue dye and a TC20 automated cell counter (Bio-Rad, Hercules, CA, USA).

2.2. Isolation of neutrophil-like cells

A total of 1.0×10^7 cells suspended in 100 μL of phosphate-buffered saline (PBS) containing 2% FBS were stained with a cocktail containing APC/Cyanine7 anti-human CD11c (1:100, Biolegend, San Deigo, CA, USA) and propidium iodide (PI, 1:100, Sigma-Aldrich), and incubated in the dark on ice for 15 min. The cells were washed with 2 mL of PBS containing 2% FBS, centrifuged at 1000×*g* for 5 min, resuspended in 1 mL of PBS containing 2% FBS, and then filtered using a cell strainer (70 μm, Corning, NY, USA). CD11c$^+$/PI$^-$ cells were sorted via fluorescence-activated cell sorting (FACS) using AriaIIIu (BD Bioscinence, Franklin Lakes, NJ, USA) with an 85 μm diameter nozzle.

2.3. Analysis of extracellular metabolites

Glucose and lactate concentrations in the culture media were measured using high-performance liquid chromatography (HPLC), as described previously (Okahashi et al., 2015). The amino acid concentrations in the culture media were measured via HPLC using the AccQ tag method (Armenta et al., 2010). An HPLC Prominence system (Shimadzu, Kyoto, Japan) equipped with a Luna C18 (2) column (250 mm, 4.6 mm, 5.0 μm, Phenomenex, Torrance, CA, USA) and a photodiode array detector was used. Derivatized amino acids were eluted using (A) 20 mM sodium acetate solution containing 0.04% (v/v) trimethylamine and phosphate adjusted to pH 6.8 and (B) acetonitrile. The following gradient program was employed: 0 min 0% (B); 0.5 min 8% (B); 17.5 min 12% (B); 19 min 15% (B); 20 min 20% (B); 30.6 min 100% (B); 33.1 min 0% (B); and 46 min 0% (B) at a flow rate of 1.0 mL/min. The absorbance was monitored at 260 nm. Column oven temperature was maintained at 40 °C.

2.4. ^{13}C-labeling analysis of intracellular metabolites

Cultured cells were quickly isolated from the culture media via vacuum filtration using an Omnipore Membrane Filter (47 mm diameter, 0.45 μm pore diameter, polytetrafluoroethylene membrane, Merck Millipore, Burlington, MA, USA), and washed with 5 mL of PBS. The filters were immersed in 500 μL of cold methanol in a centrifuge tube and stored at −80 °C. Quenching was performed for 15 s. Intracellular metabolites were extracted via the addition of 500 μL of chloroform and 200 μL of Milli-Q water. The mixed solution was vortexed for 1 min and centrifuged at 2580×*g* for 20 min at 4 °C. After a 10-min incubation at 4 °C, the upper layer was transferred to an Eppendorf tube, and evaporated to dryness using a centrifugal evaporator (CVE-2100, EYELA, Tokyo, Japan) at room temperature. ^{13}C-labeling of intracellular metabolites was measured using gas chromatography-mass spectrometry (GC-MS) via methoxyamination and *tert*-butyldimethylsilyl derivatization (Okahashi et al., 2022), and ion-pair liquid chromatography-tandem mass spectrometry (ion-pair LC-MS/MS). For GC-MS analysis, dried metabolites were dissolved in 25 μL of 40 mg/mL methoxyamine hydrochloride in pyridine and incubated for 60 min at 30 °C. A 25-μL volume of *N*-methyl-*N*-(*tert*-butyldimethylsilyl)

trifluoroacetamide containing 1% *tert*-butyldimethylchlorosilane was added to the solution, which was then held for 60 min at 60 °C. After 60 min of cooling and centrifugation at 15,000×*g* for 5 min, the supernatants were analyzed using a GC-MS system (GC-MS-QP2020, Shimadzu) equipped with a DB-5MS + DG capillary column (30 m, 0.25 mm, 0.25 μm, Agilent Technologies, Santa Clara, CA, USA), as described previously (Okahashi et al., 2022). For ion-pair LC-MS/MS analysis, LCMS-8050 triple quadrupole mass spectrometry (Shimadzu) equipped with a MASTRO C18 column (150 mm, 2.1 mm, 3.0 μm, Shimadzu GLC, Tokyo, Japan) was operated using the methods package for primary metabolites Ver.2 (Shimadzu). The following parameters were employed for the analysis: MS analysis mode, negative ion mode; electrospray voltage, 4.0 kV; desolvation line, 250 °C; heat block temperature, 400 °C; nebulizing gas (N_2) flow, 3.0 L/min; drying gas (N_2) flow, 15.0 L/min; and collision-induced dissociation (Ar) pressure, 0.27 MPa. The derivatized metabolites (1 μL) were injected and eluted in (A) 15 mM acetate solution containing 10 mM tributylamine and (B) methanol using the following gradient program: 0 min 0% (B); 8 min 25% (B); 12 min 98% (B); 15.1 min 0% (B); and 20 min 0% (B) at a flow rate of 0.3 mL/min. The column oven temperature was maintained at 40 °C. Fraction labeling of the metabolites was determined as described previously (Okahashi et al., 2022).

2.5. ^{13}C-metabolic flux analysis

A metabolic network model consisting of 111 reactions and 55 metabolites, including glycolysis, PPP, TCA cycle, anaplerosis, amino acid metabolism, and transport reactions between the cytoplasm and mitochondria, was used (Table S1). The fluxes for biomass synthesis were calculated from the precursor requirements and dry cell weight (Table S2) (Sheikh et al., 2005). Based on the experimental results, the dry cell weight of HL-60 was 1.2×10^{-10} g/cells. Metabolic fluxes were calculated by mfapy (Matsuda et al., 2021) using Python 3.6, with numpy-1.9, scipy-0.13.2, and pyOpt-1.2.0. ^{13}C-labeling of each metabolite was determined using the elementary metabolite unit framework (Antoniewicz et al., 2007). The effects of naturally occurring isotopes were removed from the raw mass spectrometry data (Okahashi et al., 2022; Van Winden et al., 2002). The metabolic flux distribution was estimated by minimizing the RSS between the experimental and simulated values of ^{13}C-labeling and influx/efflux, using the following equation (eq1):

$$RSS = \sum_{j=1}^{N} \left(\frac{MDV_j^{exp} - MDV_j^{sim}}{\sigma_j} \right)^2 + \sum_{k=1}^{M} \left(\frac{r_k^{exp} - r_k^{sim}}{\sigma_k} \right)^2 \quad \text{(eq1)}$$

where MDV_j^{exp}/r_k^{exp} and MDV_j^{sim}/r_k^{sim} represent the experimentally measured and simulated mass isotopomer distribution vector (MDV) of the *j*-th metabolite and *k*-th influx/efflux, respectively, and σ_j and σ_k indicate the standard deviation of MDV and influx/efflux of measured data. Similar to a previous study (Araki et al., 2018) , σ_j was assumed to be 0.01. Sequential least squares programming (SLSQP), a nonlinear optimization solver, was initiated from 1000 datasets with initial values. χ^2 tests were conducted to evaluate the goodness of the fit of the experimental data to the metabolic model. The threshold value was determined via χ^2 distributions at a significance level of 5%. The 95% confidence intervals of the flux values were calculated using the grid-search method (Antoniewicz et al., 2006). To determine ATP regeneration flux via OXPHOS, the P/O ratio was set to 2.3 (Hinkle, 2005).

3. Results

3.1. Metabolic alterations via differentiation and immune activation

To characterize metabolic alterations via cellular differentiation and immune activation, HL-60 cells were differentiated into resting neutrophil-like cells via culture with 1 μM retinoic acid for 6 days (Fig. 1A). Differentiation was evaluated based on the expression level of CD11c, a granulocyte-specific integrin, and PI staining of dead cells using flow cytometry. $CD11c^+/PI^-$ cells increased to 37.2% via induction of differentiation (Fig. 1B). The $CD11c^+/PI^-$ population was assumed to be differentiated HL-60 (dHL-60) cells and was sorted via FACS for the ROS production assay. PMA stimulation increased ROS-induced Rhodamine 123 fluorescence in dHL-60 cells compared to undifferentiated HL-60 cells. (Fig. 1C), demonstrating that dHL-60 cells had a proper neutrophil function. Thereafter, the immune response was induced via LPS stimulation (Fig. 1A).

To determine the effect of cell state transition on metabolism, HL-60, dHL-60, and LPS-stimulated dHL-60 (LPS-dHL-60) cells were cultured in RPMI 1640 medium for 48 h. The dHL-60 and LPS-dHL-60 cells had no proliferative capacity, whereas HL-60 cells grew exponentially at a specific growth rate of 0.018 h^{-1} (Fig. 1D). Specific uptake and secretion rates were calculated using the time-course data of viable cell counts and levels of medium components measured by HPLC. The specific rates of glucose uptake and lactate secretion of HL-60 cells were 115 ± 6 and 250 ± 5 nmol/10^6 cells/h, respectively, whereas those of dHL-60 cells were 52 ± 2 and 115 ± 2 nmol/10^6 cells/h, respectively (Figs. 1E and F). Glucose uptake and lactate secretion rates decreased by 0.45- and 0.46-fold, respectively, during differentiation into neutrophil-like cells, indicating a reduction in glycolytic flux in dHL-60 cells. These data suggest that quiescent dHL-60 cells require less energy than proliferative HL-60 cells. The specific rate of glucose uptake and lactate secretion of LPS-dHL-60 cells were 78 ± 1 and 129 ± 3 nmol/10^6 cells/h, respectively (Figs. 1E and F), indicating that stimulation with LPS re-activated glycolysis in dHL-60 cells. The increase in the glucose uptake rate was greater than that of the lactate secretion rate, suggesting that LPS-dHL-60 cells directed the glucose-derived carbon flow into the TCA cycle. During the immune response, dHL-60 cells may require a large amount of energy despite the loss of proliferative capacity. The glutamine uptake rate of the three cell types was 22 ± 1, 26 ± 2, and 23 ± 2 nmol/10^6 cells/h for HL-60, dHL-60, and LPS-dHL-60 cells, respectively (Fig. 1G), indicating that the change of glutamine uptake rate was not prominent, compared to the glucose uptake and lactate secretion rates. In contrast, specific arginine uptake rates differed significantly among the three cell types (Fig. 1H). Differentiation into dHL-60 cells increased the rate of glutamate secretion (Table S3). The specific production rates of other non-essential amino acids, such as alanine, aspartate, and proline, in the three cell types were less than 5.6% of the glucose uptake (Table S3). These results indicate that dHL-60 cells had reduced dependence on glucose as a carbon source, which was partially restored by LPS stimulation.

3.2. Isotopic labeling using [U–$^{13}C_6$]glucose, [U–$^{13}C_5$]glutamine, and [U–$^{13}C_6$]arginine

Isotopic labelling experiments were performed to gain insights into the metabolic fate of the assimilated carbon sources. The three cell types were cultured in media containing [U–$^{13}C_6$]glucose, [U–$^{13}C_5$]glutamine, or [U–$^{13}C_6$]arginine, and the ^{13}C-labeling patterns of intracellular metabolites were measured using GC-MS. [U–$^{13}C_6$]glucose and [U–$^{13}C_5$]glutamine/[U–$^{13}C_6$]arginine are broken down to M+3 pyruvate and M+5 α-ketoglutarate (aKG), respectively (Fig. 2A). The fraction of M+3 pyruvate was >70% in the three cell types cultured in medium containing [U–$^{13}C_6$]glucose (Fig. S1A). The M+2 fraction of citrate biosynthesized via pyruvate dehydrogenase (PDH) was 44.7%, 24.6%, and 28.2% in HL-60, dHL-60, and LPS-dHL-60 cells, respectively (Fig. 2B), indicating that the glucose-derived carbon reached the TCA cycle. The M+5 fraction of aKG from [U–$^{13}C_5$]glutamine was 52.1%, 26.8%, and 44.0% in HL-60, dHL-60, and LPS-dHL-60 cells, respectively (Fig. 2C), indicating that the TCA cycle was also fueled by glutamine, even in neutrophil-like cells, which were considered to have fewer mitochondria

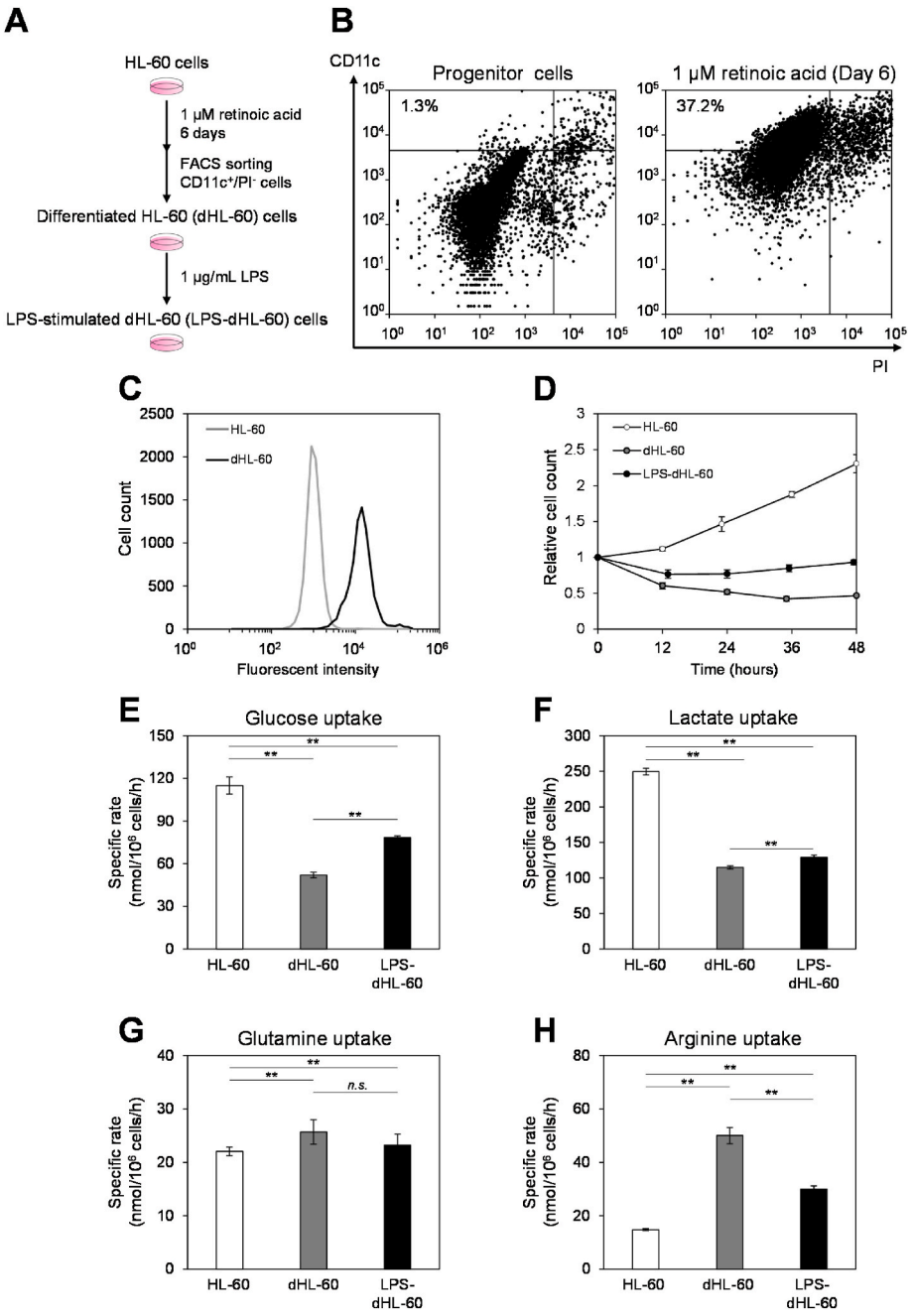

Fig. 1. Metabolic alterations among three states of HL-60 cells indicated by influx and efflux measurements. (A) Outline of the experiments. Differentiated HL-60 (dHL-60) cells were prepared via the addition of 1 μM retinoic acid to HL-60 cells. The cells were then cultured for 6 days and sorted using FACS. dHL-60 cells were activated by the addition of 1 μg/mL LPS (LPS-dHL-60). HL-60, dHL-60, and LPS-dHL-60 cells were cultured for 48 h. (B) Confirmation of the differentiation into neutrophil-like cells. (C) Measurement of ROS-producing cells using flow cytometry. The black and gray lines represent HL-60 and dHL-60 cells, respectively, treated with 125 μM PMA for 1 h. (D) Time-course of viable cell number. White, gray, and black indicate number of HL-60, dHL-60, and LPS-dHL-60 cells, respectively. Data are presented as mean ± standard deviation ($n = 3$). (E–H) Specific uptake and secretion rates of (E) glucose, (F) lactate, (G) glutamine, and (H) arginine. Data indicate the slopes of metabolite levels in media against cumulative viable cell number ($n = 13$). Error bars represent the 68% confidence interval of the slopes. **, p-value <0.01 in two-tailed Bonferroni corrected Student's t-test. *n.s.*, no significance.

(Kominsky et al., 2010). In contrast, the M+5 fraction of aKG was not detected in cells cultured with [U–$^{13}C_6$]arginine (less than 0.4%; Fig. 2D), demonstrating that arginine was not catabolized during central carbon metabolism. The total fractional ^{13}C-labeling, determined based on the sum of each fraction of [U–$^{13}C_6$]glucose and [U–$^{13}C_5$]glutamine, was less than 80% in all three cell types (Figs. 2E and S1B-D). In particular, metabolites in the TCA cycle displayed smaller fractions of ^{13}C-labeling: 58%, 41%, and 37% for citrate; 76%, 41%, and 61% for aKG; and 43%, 19%, and 30% for malate in HL-60, dHL-60, and LPS-dHL-60 cells, respectively (Figs. 2E and S1B-D). These data imply that carbon sources, besides glucose and glutamine, contribute to the TCA cycle intermediates, and this trend is remarkable in resting dHL-60 cells.

3.3. Isotopic labeling using [U–^{13}C]non-essential amino acids

The non-essential amino acids contained in the RPMI 1640 medium were expected to be metabolized in the TCA cycle. To identify unknown

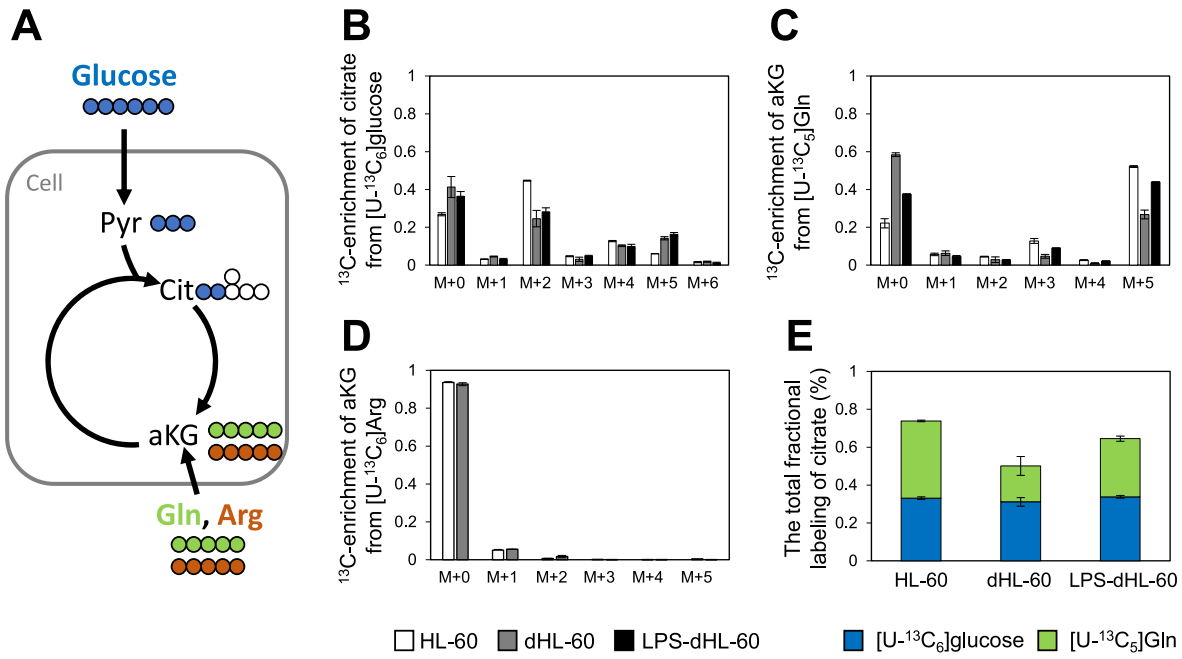

Fig. 2. Catabolism of major carbon sources. (A) Schematic of the assimilation pathways for the uptake of carbon sources. The cells were cultured for 46 h in media containing either [U–$^{13}C_6$]glucose, [U–$^{13}C_5$]glutamine, or [U–$^{13}C_6$]arginine. The ^{13}C-atom corresponding to each carbon source is depicted by a colored circle. (B–D) The labeling patterns of (B) citrate from [U–$^{13}C_6$]glucose, (C) aKG from [U–$^{13}C_5$]glutamine, and (D) aKG from [U–$^{13}C_6$]arginine in three cell types. The effects of naturally occurring isotope, except skeletal carbon, were corrected. (E) Total fractional ^{13}C-labeling of citrate from [U–$^{13}C_6$]glucose and [U–$^{13}C_5$]glutamine. All data are presented as mean ± standard deviation (n = 3).

carbon sources, HL-60, dHL-60, and LPS-dHL-60 cells were cultured in RPMI 1640 medium to replace a single non-essential amino acid with the corresponding [U–$^{13}C_4$]aspartate, [U–$^{13}C_5$]glutamate, [U–$^{13}C_3$]serine, or [U–$^{13}C_5$]proline. Asparagine was also removed when the cells were cultured in the [U–$^{13}C_4$]aspartate-containing medium. The metabolized products of these non-essential amino acids are shown in Fig. 3A. [U–$^{13}C_3$]serine and [U–$^{13}C_4$]aspartate biosynthesized M+3 pyruvate and M+4 malate, respectively, and both [U–$^{13}C_5$]glutamate and [U–$^{13}C_5$]proline biosynthesized M+5 aKG (Fig. 3A). The M+3 fraction of pyruvate from [U–$^{13}C_3$]serine was less than 1% in all cell types (Fig. 3B), indicating that serine was not broken down during central carbon metabolism. The M+5 fraction of aKG from [U–$^{13}C_5$]proline was 0.1%, 1.5%, and 3.2% in HL-60, dHL-60, and LPS-dHL-60 cells, respectively (Fig. 3C), indicating that proline is a minor carbon source that enters central carbon metabolism. In contrast, M+4 malate from [U–$^{13}C_4$]aspartate (12% in HL-60 cells, 45% in dHL-60 cells, and 44% in LPS-dHL-60 cells) and M+5 aKG from [U–$^{13}C_5$]glutamate (11% in HL-60 cells, 28% in dHL-60 cells, and 24% in LPS-dHL-60 cells) were detected (Figs. 3D and E). Interestingly, the assimilated aspartate and glutamate were constant in the media or secreted rather than consumed by the cells (Table S3). Although ^{13}C-labeling from [U–$^{13}C_4$]aspartate and [U–$^{13}C_5$]glutamate was incorporated into the TCA cycle metabolites, the total fractional labeling of citrate, aKG, and malate did not reach 100% (total fractional labeling of citrate was 84%, 76%, and 88%, respectively; that of aKG was 91%, 77%, and 93%, respectively; and that of malate was 61%, 75%, and 85% in HL-60, dHL-60, and LPS-dHL-60 cells, respectively, Figs. 3F–H). These observations imply the presence of carbon sources other than non-essential amino acids in the medium. Essential amino acids, such as branched-chain amino acids, are candidates for carbon sources. For example, the three cell types were cultured with [U–$^{13}C_6$]leucine, which was catabolized to M+2 acetyl CoA (Fig. S2A). The M+2 fraction of citrate in HL-60, dHL-60, and LPS-dHL-60 cells was 1.8%, 2.8%, and 2.6%, respectively (Fig. S2B), indicating that leucine and potentially other branched-chain amino acids were minor carbon sources for the three cell types. These data are consistent with those of a previous study, in which the uptake of essential amino acids was found to be balanced with protein synthesis flux in mammalian cells (Okahashi et al., 2015). This observation explains the absence of essential amino acid catabolism in the modified metabolic model.

3.4. *Reverse isotopic experiments from intracellular macromolecules*

Neutrophils utilize fatty acids during maturation (Curi et al., 2020). Glycogen is important in tissues far from blood vessels and media lacking glucose (Robinson et al., 1982; Sadiku et al., 2021). These previous studies suggest that neutrophili-like cells may break down macromolecules within the cells. To test this hypothesis, ^{13}C-labeled HL-60 cells were prepared by culturing in medium containing [U–$^{13}C_6$]glucose for 6 days, and the cells were further differentiated into dHL-60 cells in [U–$^{13}C_6$]glucose medium (Fig. 4A). ^{13}C-labeled HL-60, dHL-60, and LPS-dHL-60 cells were cultured in non-labeled medium for 46 h, and the ^{13}C-labeling patterns of intermediates in glycolysis, the PPP and TCA cycles were measured using GC-MS and LC-MS/MS. The metabolized products from ^{13}C-labeled biomass are shown in Fig. 4B. Although the M+6 fraction of G6P was less than 1% in all cell types (Fig. 4C), the M+5 fraction of R5P was >10% in dHL-60 and LPS-dHL-60 cells (Fig. 4D). Such finding indicates that dHL-60 cells did not metabolize glycogen but metabolized nucleic acids. The M+2 fraction of citrate was 18.2%, 40.9%, and 31.2% in HL-60, dHL-60, and LPS-dHL-60 cells, respectively, whereas the M+3 fraction of pyruvate was <3% (Figs. 4E and F), demonstrating that all cells drove fatty acid oxidation (FAO). These data are consistent with those of previous studies, in which differentiated cells were found to shift their glycolytic metabolism toward FAO utilization (Namgaladze and Brüne, 2016; O'Sullivan et al., 2014).

3.5. *^{13}C-metabolic flux analysis of the three cell types*

To quantitatively characterize metabolic reprogramming through differentiation and immune response, ^{13}C-metabolic flux analysis was performed via the culture of HL-60, dHL-60, and LPS-dHL-60 cells in media containing [1,2–$^{13}C_2$]glucose for 48 h. For dHL-60 cells, [U–$^{13}C_5$] glutamine was added to the medium owing to the minimal contribution

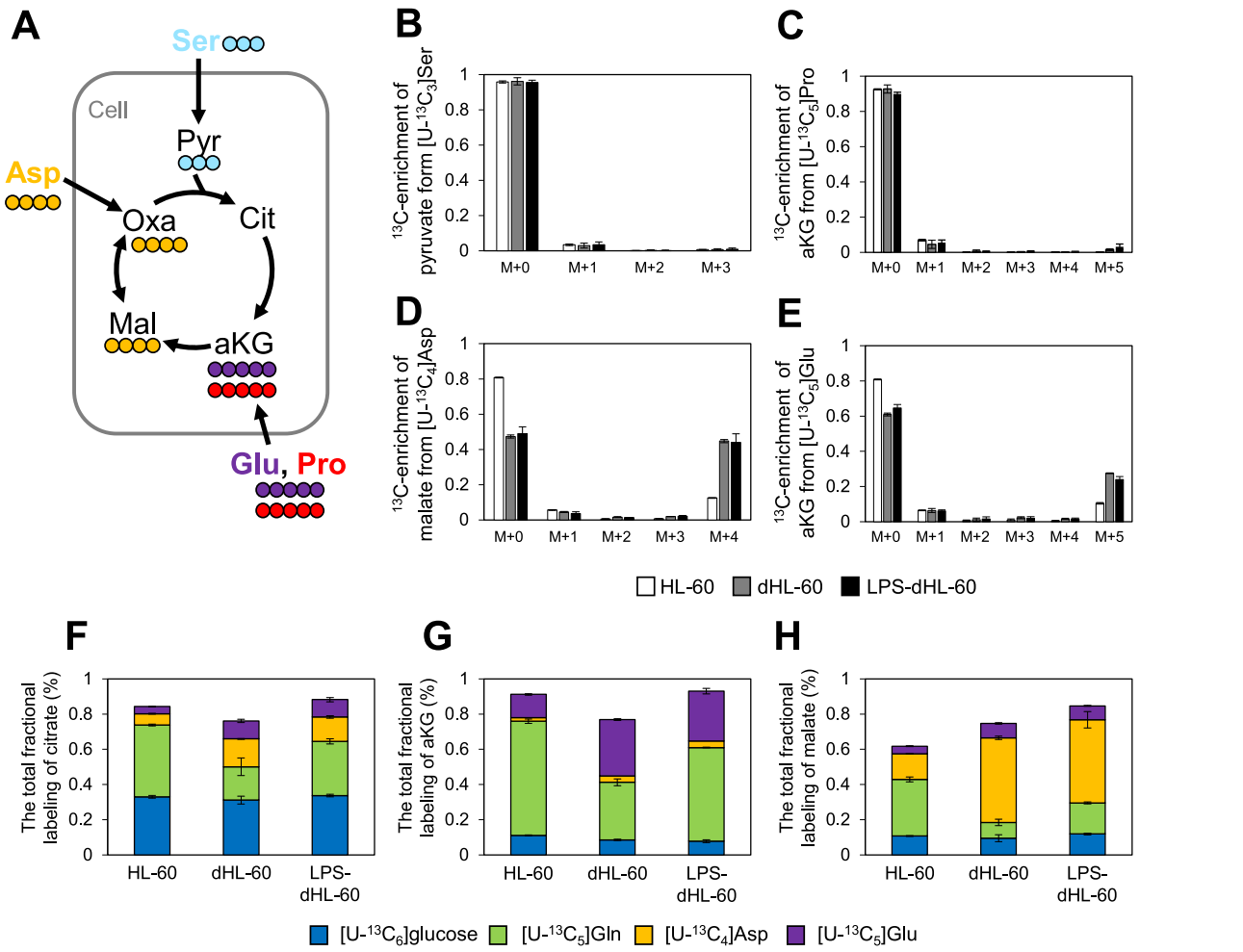

Fig. 3. Assimilation of non-essential amino acids. (A) Schematic of the assimilation pathways of extracellular non-essential amino acids. (B–E) Labeling patterns of (B) pyruvate from [U–$^{13}C_3$]serine, (C) aKG from [U–$^{13}C_5$]proline, (D) malate from [U–$^{13}C_4$]aspartate, and (E) aKG from [U–$^{13}C_5$]glutamate in the three cell types. The effects of naturally occurring isotope, except skeletal carbon, were corrected. (F–H) Total fractional ^{13}C-labeling of (F) citrate, (G) aKG, and (H) malate from [U–^{13}C]carbon sources. All data are presented as mean ± standard deviation (n = 3).

of glucose to the TCA cycle (Figs. 1E, and S1B-D). An isotopically stationary state was observed at 36–48 h (Fig. S3). Metabolic flux distributions were calculated using mfapy software (Matsuda et al., 2021), the influx/efflux of extracellular metabolites, and ^{13}C-labeling of intracellular metabolites (Fig. S3, Tables S3 and S4). Metabolic steady states were confirmed for three cell types by the linearity of the plots of nutrient amounts versus cumulative viable cell numbers (Fig. S4).

First, metabolic flux distribution was estimated using the original metabolic model for cancer cells (Fig. 5A) (Okahashi et al., 2019). The RSS values of HL-60, dHL-60, and LPS-dHL-60 cells were 530, 9780, and 550, respectively, which were higher than the statistically acceptable thresholds (55 for HL-60 cells, 43 for dHL-60 cells, and 51 for LPS-dHL-60 cells) for the three cell types (Figs. 5E–G). Such finding indicates that this metabolic model was not suitable for ^{13}C-metabolic flux analysis of neutrophil-like cells. Second, based on the data in Figs. 2 and 3, the original metabolic model was modified by adding glutamate, proline, and aspartate uptake, and omitting arginine uptake in the medium (Fig. 5B). The exchange fluxes of extracellular glutamate, proline, and aspartate were modeled as free parameters by constraining the net fluxes using the measured efflux. Correcting for either the amino acid influx into aKG or oxaloacetate in the original metabolic model (Figs. S5A and B) did not yield a statistically acceptable RSS for any cell types (Figs. S5C-E). Modification of both amino acid metabolism reactions decreased the RSS of HL-60, dHL-60, and LPS-dHL-60 cells to 33, 302, and 39, respectively, demonstrating that the modified metabolic model produced a statistically acceptable RSS for HL-60 and LPS-dHL-60 cells, whereas dHL-60 cells still had higher the RSS than the threshold (Figs. 5E–G). Finally, the degradation reactions of fatty acids and nucleic acids shown in Fig. 4 were added to the modified metabolic model (Figs. 5C and D). The exchange fluxes of fatty acids and nucleic acids were modeled as free parameters by constraining the net fluxes to biomass synthesis rate. The newly developed metabolic model of HL-60 cells (Figs. 5C) did not include the breakdown of nucleic acids owing to the absence of ^{13}C-labeling R5P in ^{13}C-labeled cells (Fig. 4D). The χ^2 tests revealed that the RSS of HL-60, dHL-60, and LPS-dHL-60 cells was 27.9, 36.1 and 28.1, respectively, and the addition of the uptake of extracellular amino acids and intracellular macromolecules to the original model allowed the RSS of all cell types to be below the statistically acceptable thresholds (49.8 for HL-60 cells, 36.4 for dHL-60 cells, 45.0 for LPS-dHL-60 cells, Figs. 5E–G, and Table S5).

The flux distribution in undifferentiated HL-60 cells was characterized using the developed metabolic model (Fig. 6A and Table S6). As a result, 90% and 9% of the incorporated glucose were found to be metabolized via glycolysis and the oxidative PPP, respectively. The yield of lactate/glucose was 191%, demonstrating that HL-60 cells were undergoing aerobic glycolytic metabolism. The flux from glutamine to aKG (16 nmol/10^6 cells/h) was comparable to the flux from pyruvate to citrate (PDH flux, 13 nmol/10^6 cells/h and pyruvate carboxylase (PC) flux, 3.6 nmol/10^6 cells/h), indicating that the TCA cycle was driven by glucose- and glutamine-derived carbon. The rate of fatty acid

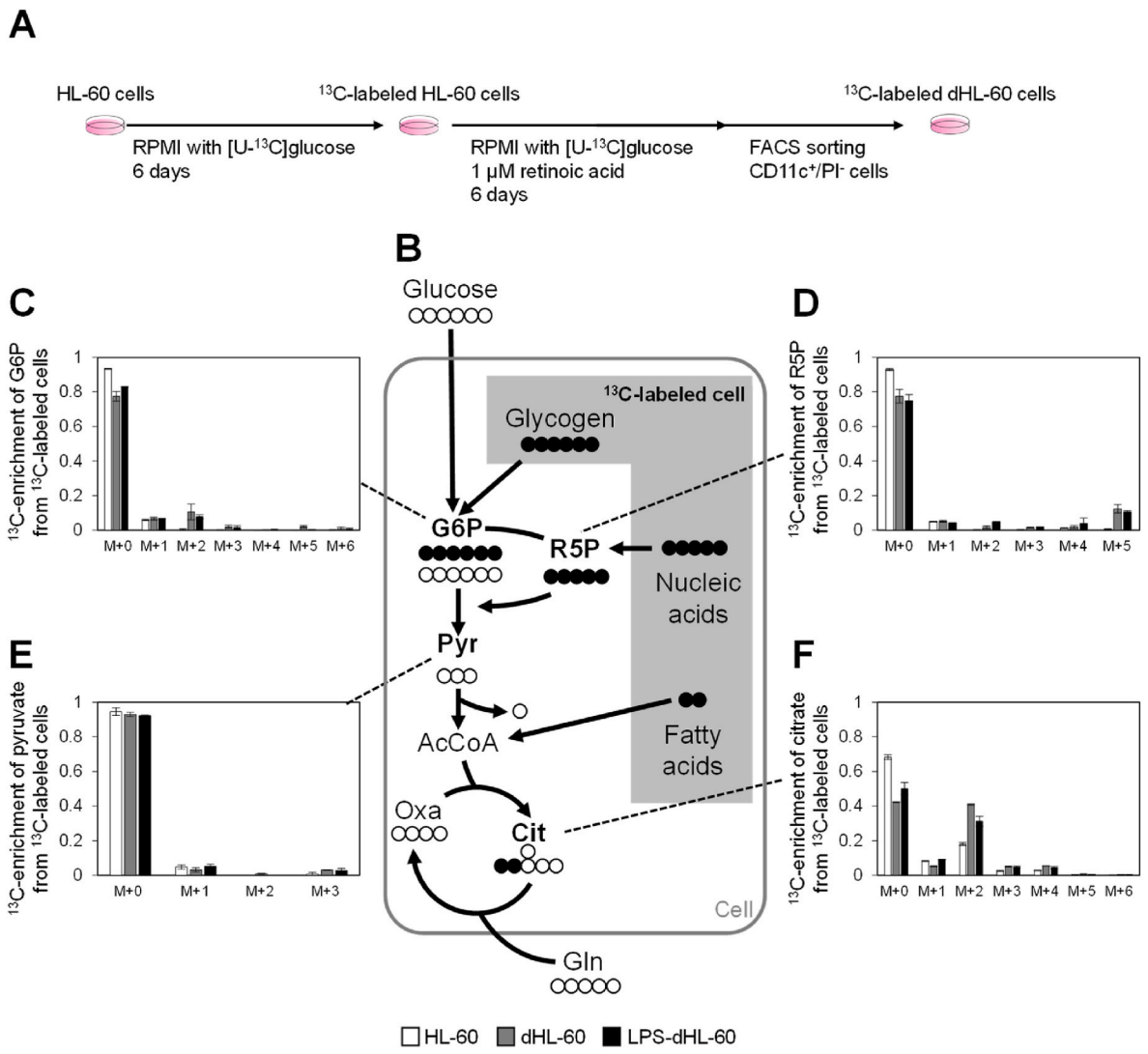

Fig. 4. Reverse isotopic labeling experiments from cellular macromolecules. (A) Schematic of the preparation procedure for ^{13}C-labeled cells. (B–F) ^{13}C-labeling of the intermediates from ^{13}C-labeled cells cultured in medium containing non-labeled carbon sources for 46 h. The effects of naturally occurring isotopes, except for skeletal carbon, were corrected. (B) Schematic of the intracellular macromolecule assimilation pathways. The white and black circles represent ^{12}C and ^{13}C, respectively. (C–D) Labeling patterns of (C) glucose-6-phosphate (G6P), (D) ribose-5-phosphate (R5P), (E) pyruvate, and (F) citrate from ^{13}C-labeled cells in the three cell types. All data are expressed as mean ± standard deviation (n = 3).

degradation was 9.9% of the total influx into the TCA cycle. The flux of the last glycolytic reaction, pyruvate kinase (PK), was 16-fold higher than the entry flux of the TCA cycle, citrate synthase (CS), highlighting high glycolytic metabolism in undifferentiated HL-60 cells.

The flux distribution in HL-60 cells was compared to that in dHL-60 cells (Fig. 6B, and Table S6). Differentiation into neutrophils reduced the glucose uptake rate and phosphofructokinase flux, the rate-limiting step of glycolysis (Tanner et al., 2018), by 0.43- and 0.48-fold, respectively. Although the total ATP regeneration rate of dHL-60 cells was 0.84-fold lower than that of HL-60 cells (Fig. 6D), the decrease was not as large as that in glycolytic flux, indicating that differentiation into neutrophils relied on OXPHOS-dependent ATP regeneration. Flux through IDH increased by 2.0-fold owing to the decrease in ATP citrate lyase (ACLY) flux. Although the best-fit flux of the oxidative PPP was 0 nmol/10^6 cells/h, the changes were not significant owing to the overlapping confidence intervals between HL-60 and dHL-60 cells. The flux of another NADPH-regenerating pathway, ME, was not significantly changed.

The addition of LPS to dHL-60 cells increased the glucose uptake rate by 1.4-fold, while the glucose-6-phosphate isomerase (GPI) flux, the second reaction of glycolysis, remained approximately the same (Fig. 6C, and Table S6). The increased carbon flux flowed into the PPP. The TCA cycle flux was markedly altered by the addition of LPS. Compared to dHL-60 cells, the FAO and CS fluxes of LPS-dHL-60 cells increased by 9.4-fold and 2.2-fold, respectively; however, the IDH and aKGDH fluxes did not significantly differ owing to overlapping confidence intervals. The malate produced by ACLY fueled the latter part of the TCA cycle and ME reaction via skipping decarboxylation reactions in the TCA cycle. The total ATP regeneration rate of LPS-dHL-60 cells did not differ from that of dHL-60 cells because the confidence interval of LPS-dHL-60 cells overlapped with that of dHL-60 cells (Fig. 6D). In contrast, the total NADPH regeneration rate of LPS-dHL-60 cells was 3.0-fold higher than that of untreated dHL-60 cells (Fig. 6E), suggesting that LPS-dHL-60 cells activated NADPH turnover for ROS production. The contribution to NADPH regeneration in LPS-dHL-60 cells was the largest in the PPP, and to the same extent, in the ME and IDH reactions.

4. Discussion

In this study, ^{13}C-metabolic flux analysis was performed using HL-60

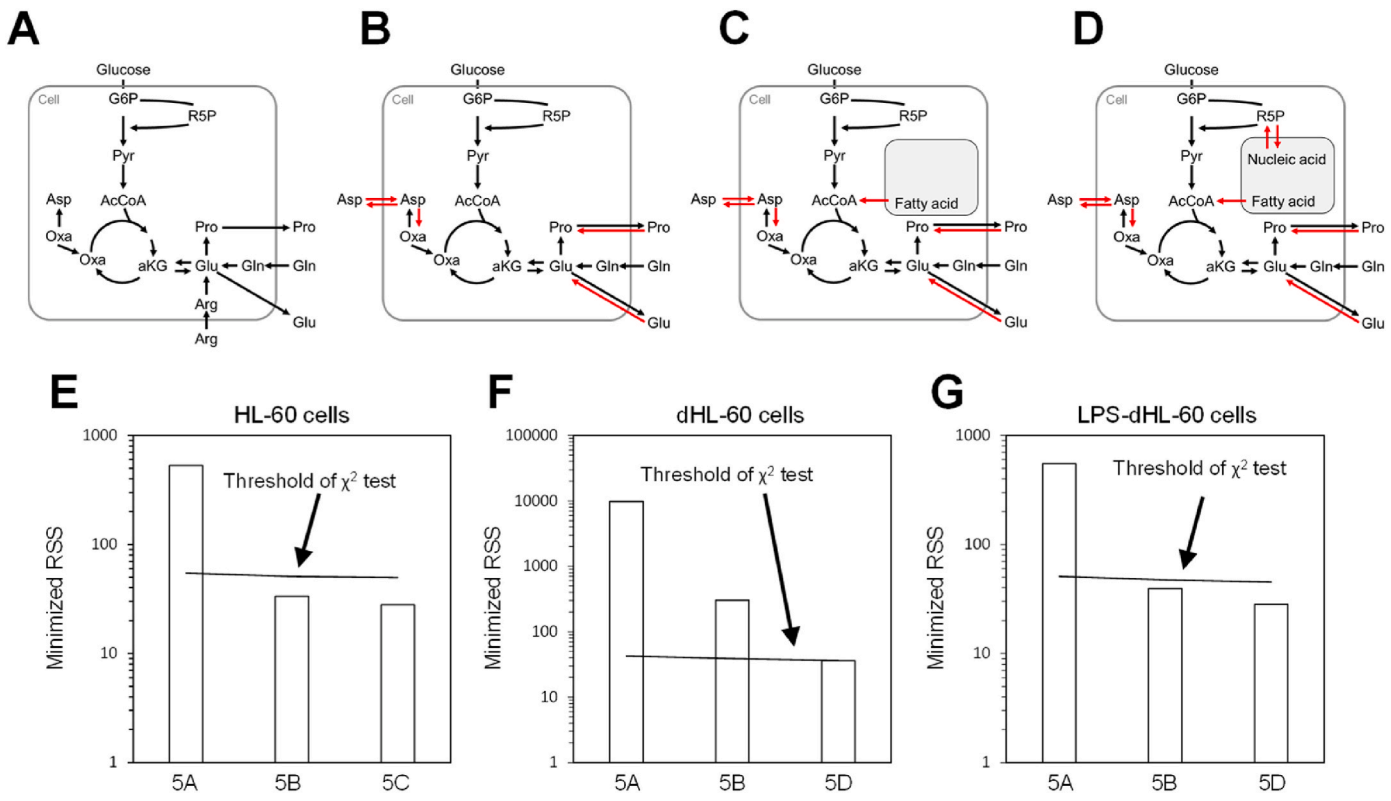

Fig. 5. Examination of the metabolic models. (A) Original model. (B–D) Modified models with the assimilation reactions of (B) amino acids, (C) fatty acids, and (D) fatty acids and nucleic acids. Red arrows indicate additional pathway to the original model. Arginine uptake was eliminated from all models. (E–G) RSS of (E) HL60, (F) dHL-60, and (G) LPS-dHL-60 calculated using the modified metabolic model shown in panels (A)-(D). Black lines indicate the threshold of the χ^2 test in each metabolic model. (For interpretation of the references to color in this figure legend, the reader is referred to the Web version of this article.)

cells, a neutrophil model cell line. Evaluation of the metabolic model revealed that carbons from aspartate and glutamate in the media, and R5P and AcCoA derived from intracellular macromolecules flowed into central carbon metabolism. ^{13}C-metabolic flux analysis was used to characterize quantitative metabolic shifts via differentiation and immune responses.

As ^{13}C-metabolic flux analysis has been developed for microorganisms such as *E. coli* and yeast, the analytes are often exponentially growing cells cultured in a medium containing a single or a few carbon sources (Wiechert, 2001). Recently, ^{13}C-metabolic flux analysis of mammalian cells has been performed in relatively rich media containing amino acids; however, catabolism into central carbon metabolism has not been well investigated, except for glutamine. In particular, the RPMI 1640 used in this study contained non-essential amino acids that were not present in Dulbecco's modified Eagle medium, which is generally used for cancer cell lines. This study highlights that the catabolism of non-essential amino acids into central carbon metabolism is independent of net uptake and secretion. Some amino acids, such as arginine, did not enter central carbon metabolism, even if their uptake rate was significant (Figs. 1H and 2D). In contrast, aspartate-derived carbons flowed into central carbon metabolism, while their concentration in the medium remained almost constant (Fig. 3D, and Table S3). Notably, glutamate-derived carbons entered central carbon metabolism despite being secreted (Fig. 3E, and Table S3), suggesting that intracellular and extracellular aspartate and glutamate were constantly exchanged. A reverse ^{13}C-labeling experiment also revealed that the three cell types utilized intracellular fatty acids and nucleic acids (Fig. 4). Isotope stationarity was observed at 36–48 h (Fig. S3), and all cells had sufficient storage to maintain the influx of fatty acids and nucleic acids. Although the need for fatty acid oxidation in neutrophil differentiation and functions have been highlighted (Fan and Ley, 2017; Riffelmacher et al., 2017), the significance of nucleic acid degradation remains unclear. mRNA decay in T cells is necessary for early differentiation (Akiyama et al., 2021; Ito-Kureha et al., 2020) and suppression of aberrant immune responses (Matsushita et al., 2009). mRNA degradation in neutrophil-like cells may support differentiation and functions, as well as homoeostatic turnover and mRNA quality control. Evidence of glycogen degradation, which is generally used by neutrophils (Sadiku et al., 2021), was not observed, probably due to the presence of glucose in this culture system.

^{13}C-metabolic flux analysis revealed the rewiring of central carbon metabolism in HL-60 cells via differentiation and immune responses. Recent studies have shown that metabolism is markedly altered via cell differentiation (Hsu et al., 2016; Oates and Antoniewicz, 2022). Many cell types, such as neurons and cardiac cells, rely on OXPHOS to obtain energy as they differentiate (Agostini et al., 2016; Leone and Kelly, 2011). In general, cells that differentiate from stem cells regenerate most of their energy via OXPHOS (Hsu et al., 2016; Xu et al., 2013; Zhang et al., 2011). In this study, ATP regeneration in HL-60 cells shifted from glycolysis to OXPHOS via differentiation (Fig. 6D), which is consistent with the previous studies, in which the metabolic pathways for energy acquisition were switched in pluripotent stem cells (Teslaa and Teitell, 2015). However, quantitative analysis revealed that the flux of the TCA cycle remained almost constant, whereas the flux levels of glycolysis decreased with differentiation (Figs. 6A and B), resulting in an increase in the relative contribution of OXPHOS to ATP regeneration. This unique observation from ^{13}C-metabolic flux analysis highlights that the metabolic shift associated with differentiation is not a two-alternative model of glycolysis and OXPHOS in HL-60 cells. Although whether this metabolic rewiring through differentiation can be applied to a broad range of cell types before and after differentiation is unclear, as HL-60 cells are cancerous cells, the application of ^{13}C-metabolic flux analysis to other cell types, such as primary cells is expected to provide a general insight into the relationship between differentiation and metabolism.

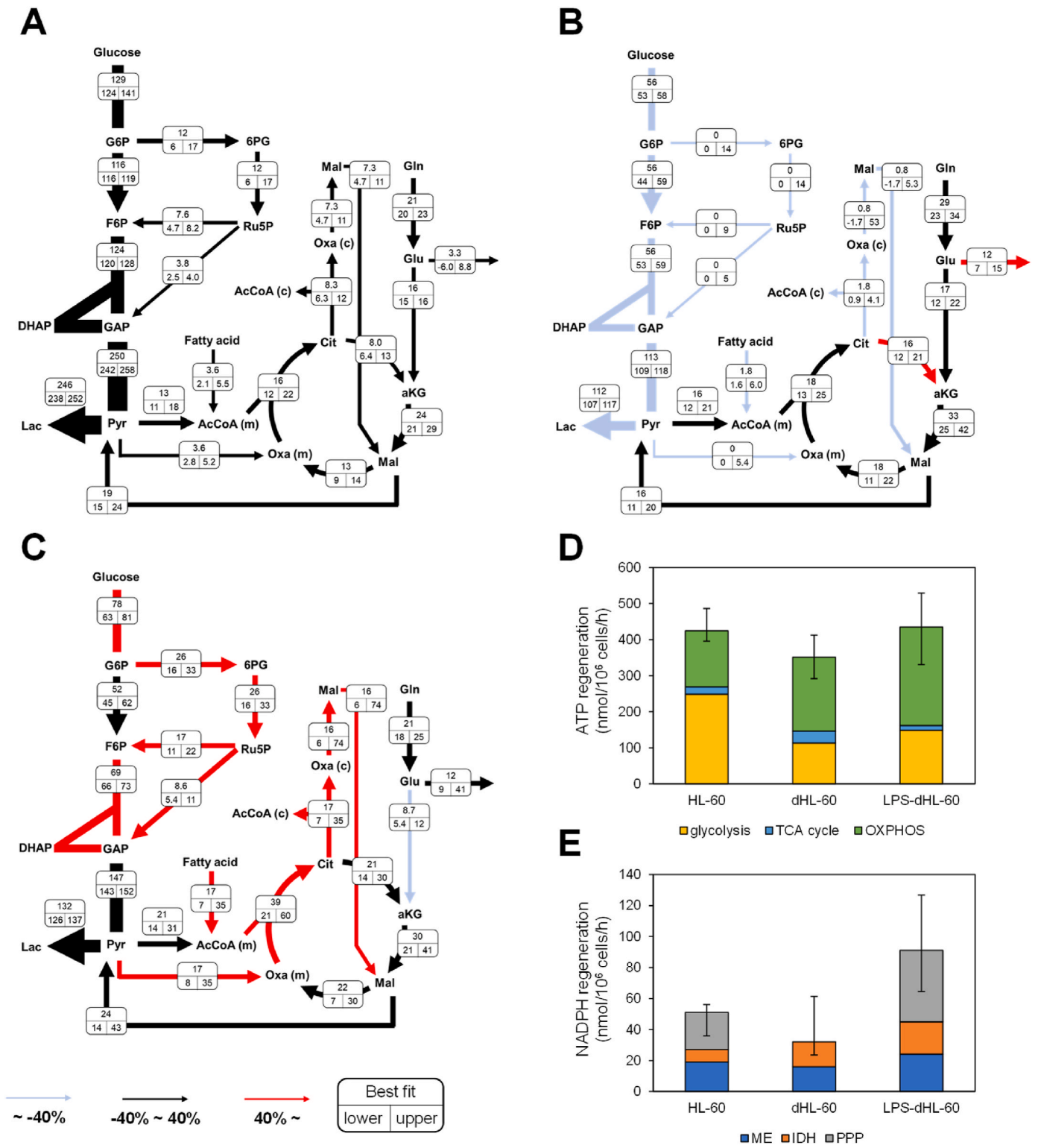

Fig. 6. ^{13}C-metabolic flux analysis of HL-60 in three states. (A–C) Flux distributions of (A) HL-60, (B) dHL-60, and (C) LPS-dHL-60 cells. The red and blue arrows indicate that the best fit value of the flux increased or decreased by more than 40% in dHL-60 cells relative to HL-60 cells, or LPS-dHL-60 cells relative to dHL-60 cells. (D, E) Total regeneration rates of (D) ATP and (E) NADPH calculated based on metabolic flux distribution of the three cell types. Error bars represent 95% confidential intervals of the total regeneration rates of ATP and NADPH. (For interpretation of the references to color in this figure legend, the reader is referred to the Web version of this article.)

The addition of LPS to dHL-60 cells increased glucose uptake, and the increased carbon flux flowed into the PPP, resulting in increased NADPH regeneration (Figs. 6C and E). Other studies have shown that T cells and macrophages activate glycolytic flux for the immune response (Buck et al., 2015; Galván-Peña and O'Neill, 2014; MacIver et al., 2013). Although activation was thought to be involved in energy acquisition, the ATP regeneration rate of LPS-dHL-60 cells was not significantly different from that of dHL-60 cells (Fig. 6D) as the increase in glucose

uptake flowed into the PPP (Figs. 6B and C). These data suggest that, unlike other immune cells, neutrophils increase their glucose uptake rate to regenerate NADPH for ROS production rather than acquire energy. The PPP activation in LPS-dHL-60 cells was milder than that in primary human neutrophils after several minutes of PMA treatment (Britt et al., 2022). This result may be due to differences in cell types, immune inducers, and assay time points. Although the activation of NADPH oxidase occurs within several minutes, metabolic rewiring continued for 48 h after LPS stimulation. Furthermore, LPS addition altered lipid metabolism, with changes in the flux levels of the TCA cycle (Fig. 6C). Lipid metabolism is essential for neutrophil differentiation and the immune response. Recent studies revealed that lipid synthesis is necessary for the biosynthesis of various inflammatory mediators and the maintenance of cell membrane composition (Bozza et al., 2009; Dennis and Norris, 2015; Lodhi et al., 2015) and the degradation of neutral lipids promotes the synthesis of lipid mediators (Zechner et al., 2017), providing additional knowledge regarding the importance of the TCA cycle as a starting and ending point for lipid metabolism in neutrophils. In summary, this study elucidated quantitative metabolic rewiring via differentiation and immune responses in neutrophil-like cells using ^{13}C-metabolic flux analysis with an optimized metabolic model.

CRediT authorship contribution statement

Takeo Taniguchi: Writing – original draft, Visualization, Validation, Investigation, Funding acquisition, Formal analysis, Data curation, Conceptualization. **Nobuyuki Okahashi:** Writing – review & editing, Writing – original draft, Project administration, Investigation, Funding acquisition, Data curation, Conceptualization. **Fumio Matsuda:** Writing – review & editing, Project administration, Data curation, Conceptualization.

Declaration of competing interest

The authors declare that there are no competing interests.

Data availability

Data are available in supplementary files.

Acknowledgements

We thank Yuki Ito and Junko Iida from Shimadzu Corporation for their support with LC-MS/MS analysis. This work was partially supported by JSPS KAKENHI [grant number 20K15100], JST GteX [grant number JPMJGX23B4], and an Extramural Collaborative Research Grant of Cancer Research Institute of Kanazawa University for N.O., and JST, the establishment of university fellowships towards the creation of science technology innovation, [grant number JPMJFS2125] for T.T.

Appendix A. Supplementary data

Supplementary data to this article can be found online at https://doi.org/10.1016/j.mec.2024.e00239.

References

Agostini, M., Romeo, F., Inoue, S., Niklison-Chirou, M.V., Elia, A.J., Dinsdale, D., Morone, N., Knight, R.A., Mak, T.W., Melino, G., 2016. Metabolic reprogramming during neuronal differentiation. Cell Death Differ. 23, 1502–1514. https://doi.org/10.1038/cdd.2016.36.

Akiyama, T., Suzuki, T., Yamamoto, T., 2021. RNA decay machinery safeguards immune cell development and immunological responses. Trends Immunol. 42, 447–460. https://doi.org/10.1016/j.it.2021.03.008.

Amador-Noguez, D., Feng, X.J., Fan, J., Roquet, N., Rabitz, H., Rabinowitz, J.D., 2010. Systems-level metabolic flux profiling elucidates a complete, bifurcated tricarboxylic acid cycle in Clostridium acetobutylicum. J. Bacteriol. 192 (4452), 4452–4461. https://doi.org/10.1128/JB.00490-10.

Antoniewicz, M.R., 2018. A guide to ^{13}C metabolic flux analysis for the cancer biologist. Exp. Mol. Med. 50 (4 50), 1–13. https://doi.org/10.1038/s12276-018-0060-y, 2018.

Antoniewicz, M.R., Kelleher, J.K., Stephanopoulos, G., 2007. Elementary Metabolite Units (EMU): a novel framework for modeling isotopic distributions. Metab. Eng. 9, 68–86. https://doi.org/10.1016/J.YMBEN.2006.09.001.

Antoniewicz, M.R., Kelleher, J.K., Stephanopoulos, G., 2006. Determination of confidence intervals of metabolic fluxes estimated from stable isotope measurements. Metab. Eng. 8, 324–337. https://doi.org/10.1016/J.YMBEN.2006.01.004.

Araki, C., Okahashi, N., Maeda, K., Shimizu, H., Matsuda, F., 2018. Mass spectrometry-based method to study inhibitor-induced metabolic redirection in the central metabolism of cancer cells. Mass Spectrom. 7, A0067. https://doi.org/10.5702/massspectrometry.a0067.

Ardati, K.O., Bajakian, K.M., Tabbara, K.S., 1997. Effect of glucose-6-phosphate dehydrogenase deficiency on neutrophil function. Acta. Haematol. 97, 211–215. https://doi.org/10.1159/000203685.

Armenta, J.M., Cortes, D.F., Pisciotta, J.M., Shuman, J.L., Blakeslee, K., Rasoloson, D., Ogunbiyi, O., Sullivan, D.J., Shulaev, V., 2010. Sensitive and rapid method for amino acid quantitation in malaria biological samples using AccQ • Tag ultra performance liquid chromatography-electrospray ionization-MS/MS with multiple reaction monitoring. Anal. Chem. 82, 548–558. https://doi.org/10.1021/ac901790q.

Awasthi, D., Nagarkoti, S., Sadaf, S., Chandra, T., Kumar, S., Dikshit, M., 2019. Glycolysis dependent lactate formation in neutrophils: a metabolic link between NOX-dependent and independent NETosis. Biochim. Biophys. Acta, Mol. Basis Dis. 1865, 165542 https://doi.org/10.1016/J.BBADIS.2019.165542.

Borregaard, N., Herlin, T., 1982. Energy metabolism of human neutrophils during phagocytosis. J. Clin. Invest. 70, 550–557. https://doi.org/10.1172/JCI110647.

Bozza, P.T., Magalhães, K.G., Weller, P.F., 2009. Leukocyte lipid bodies - biogenesis and functions in inflammation. Biochim. Biophys. Acta 1791, 540–551. https://doi.org/10.1016/J.BBALIP.2009.01.005.

Breitman, T.R., Selonick, S.E., Collins, S.J., 1980. Induction of differentiation of the human promyelocytic leukemia cell line (HL-60) by retinoic acid. Proc. Natl. Acad. Sci. U S A. 77, 2936–2940. https://doi.org/10.1073/PNAS.77.5.2936.

Britt, E.C., Lika, J., Giese, M.A., Schoen, T.J., Seim, G.L., Huang, Z., Lee, P.Y., Huttenlocher, A., Fan, J., 2022. Switching to the cyclic pentose phosphate pathway powers the oxidative burst in activated neutrophils. Nat. Metab. 4, 389–403. https://doi.org/10.1038/s42255-022-00550-8.

Buck, M.D., O'Sullivan, D., Pearce, E.L., 2015. T cell metabolism drives immunity. J. Exp. Med. 212, 1345–1360. https://doi.org/10.1084/JEM.20151159.

Burn, G.L., Foti, A., Marsman, G., Patel, D.F., Zychlinsky, A., 2021. The neutrophil. Immunity 54, 1377–1391. https://doi.org/10.1016/J.IMMUNI.2021.06.006.

Crown, S.B., Antoniewicz, M.R., 2013. Publishing ^{13}C metabolic flux analysis studies: a review and future perspectives. Metab. Eng. 20, 42–48. https://doi.org/10.1016/J.YMBEN.2013.08.005.

Curi, R., Levada-Pires, A.C., Borges Da Silva, E., De Oliveira Poma, S., Freitas Zambonatto, R., Domenech, P., Mendes De Almeida, M., Gritte, R.B., Souza-Siqueira, T., Gorjão, R., Newsholme, P., Pithon-Curi, T.C., 2020. The critical role of cell metabolism for essential neutrophil functions. Cell. Physiol. Biochem. 54, 629–647. https://doi.org/10.33594/000000245.

Dennis, E.A., Norris, P.C., 2015. Eicosanoid storm in infection and inflammation. Nat. Rev. Immunol. 15, 511–523. https://doi.org/10.1038/nri3859.

Fan, Z., Ley, K., 2017. Developing neutrophils must Eat…Themselves. Immunity 47, 393–395. https://doi.org/10.1016/J.IMMUNI.2017.08.013.

Galván-Peña, S., O'Neill, L.A.J., 2014. Metabolic reprograming in macrophage polarization. Front. Immunol. 5, 420. https://doi.org/10.3389/FIMMU.2014.00420.

Guntur, A.R., Gerencser, A.A., Le, P.T., DeMambro, V.E., Bornstein, S.A., Mookerjee, S. A., Maridas, D.E., Clemmons, D.E., Brand, M.D., Rosen, C.J., 2018. Osteoblast-like mc3t3-E1 cells prefer glycolysis for ATP production but adipocyte-like 3T3-L1 cells prefer oxidative phosphorylation. J. Bone Miner. Res. 33, 1052–1065. https://doi.org/10.1002/JBMR.3390.

Hinkle, P.C., 2005. P/O ratios of mitochondrial oxidative phosphorylation. Biochim. Biophys. Acta 1706, 1–11. https://doi.org/10.1016/J.BBABIO.2004.09.004.

Hsu, Y.-C., Wu, Y.-T., Yu, T.-H., Wei, Y.-H., 2016. Mitochondria in mesenchymal stem cell biology and cell therapy: from cellular differentiation to mitochondrial transfer. Semin. Cell Dev. Biol. 52, 119–131. https://doi.org/10.1016/j.semcdb.2016.02.011.

Ito-Kureha, T., Miyao, T., Nishijima, S., Suzuki, T., Koizumi, S. ichi, Villar-Briones, A., Takahashi, A., Akiyama, N., Morita, M., Naguro, I., Ishikawa, H., Ichijo, H., Akiyama, T., Yamamoto, T., 2020. The CCR4–NOT deadenylase complex safeguards thymic positive selection by down-regulating aberrant pro-apoptotic gene expression. Nat. Commun. 11, 6169. https://doi.org/10.1038/S41467-020-19975-4.

Jeon, J.H., Hong, C.W., Kim, E.Y., Lee, J.M., 2020. Current understanding on the metabolism of neutrophils. Immune. Netw 20, e46. https://doi.org/10.4110/IN.2020.20.E46.

Jiang, L., Boufersaoui, A., Yang, C., Ko, B., Rakheja, D., Guevara, G., Hu, Z., DeBerardinis, R.J., 2017. Quantitative metabolic flux analysis reveals an unconventional pathway of fatty acid synthesis in cancer cells deficient for the mitochondrial citrate transport protein. Metab. Eng. 43, 198–207. https://doi.org/10.1016/J.YMBEN.2016.11.004.

Kominsky, D.J., Campbell, E.L., Colgan, S.P., 2010. Inflammation metabolic shifts in immunity and inflammation. J. Immunol. 184, 4062–4068. https://doi.org/10.4049/jimmunol.0903002.

Kumar, S., Dikshit, M., 2019. Metabolic insight of neutrophils in health and disease. Front. Immunol. 10, 2099. https://doi.org/10.3389/FIMMU.2019.02099/BIBTEX.

Leighty, R.W., Antoniewicz, M.R., 2012. Parallel labeling experiments with [U-^{13}C] glucose validate E. coli metabolic network model for ^{13}C metabolic flux analysis. Metab. Eng. 14, 533–541. https://doi.org/10.1016/J.YMBEN.2012.06.003.

Leone, T.C., Kelly, D.P., 2011. Transcriptional control of cardiac fuel metabolism and mitochondrial function. Cold Spring Harb. Symp. Quant. Biol. 76, 175–182. https://doi.org/10.1101/SQB.2011.76.011965.

Lodhi, I.J., Wei, X., Yin, L., Feng, C., Adak, S., Abou-Ezzi, G., Hsu, F.F., Link, D.C., Semenkovich, C.F., 2015. Peroxisomal lipid synthesis regulates inflammation by sustaining neutrophil membrane phospholipid composition and viability. Cell Metab. 21, 51–64. https://doi.org/10.1016/J.CMET.2014.12.002.

Loftus, R.M., Finlay, D.K., 2016. Immunometabolism: cellular metabolism turns immune regulator. J. Biol. Chem. 291, 1–10. https://doi.org/10.1074/jbc.R115.693903.

MacIver, N.J., Michalek, R.D., Rathmell, J.C., 2013. Metabolic regulation of T lymphocytes. Annu. Rev. Immunol. 31, 259–283. https://doi.org/10.1146/ANNUREV-IMMUNOL-032712-095956.

Maianski, N.A., Geissler, J., Srinivasula, S.M., Alnemri, E.S., Roos, D., Kuijpers, T.W., 2003. Functional characterization of mitochondria in neutrophils: a role restricted to apoptosis. Cell Death Differ. 11, 143–153. https://doi.org/10.1038/sj.cdd.4401320.

Matsuda, F., Maeda, K., Taniguchi, T., Kondo, Y., Yatabe, F., Okahashi, N., Shimizu, H., 2021. mfapy: an open-source Python package for ^{13}C-based metabolic flux analysis. Metab. Eng. Commun. 13, e00177 https://doi.org/10.1016/J.MEC.2021.E00177.

Matsushita, K., Takeuchi, O., Standley, D.M., Kumagai, Y., Kawagoe, T., Miyake, T., Satoh, T., Kato, H., Tsujimura, T., Nakamura, H., Akira, S., 2009. Zc3h12a is an RNase essential for controlling immune responses by regulating mRNA decay. Nature 458, 1185–1190. https://doi.org/10.1038/nature07924.

Metallo, C.M., Walther, J.L., Stephanopoulos, G., 2009. Evaluation of ^{13}C isotopic tracers for metabolic flux analysis in mammalian cells. J. Biotechnol. 144, 167–174. https://doi.org/10.1016/J.JBIOTEC.2009.07.010.

Moiz, B., Garcia, J., Basehore, S., Sun, A., Li, A., Padmanabhan, S., Albus, K., Jang, C., Sriram, G., Clyne, A.M., 2021. ^{13}C metabolic flux analysis indicates endothelial cells attenuate metabolic perturbations by modulating TCA activity. Metabolites 11, 226. https://doi.org/10.3390/METABO11040226/S1.

Moiz, B., Sriram, G., Clyne, A.M., 2023. Interpreting metabolic complexity via isotope-assisted metabolic flux analysis. Trends Biochem. Sci. 48, 553–567. https://doi.org/10.1016/J.TIBS.2023.02.001.

Namgaladze, D., Brüne, B., 2016. Macrophage fatty acid oxidation and its roles in macrophage polarization and fatty acid-induced inflammation. Biochim. Biophys. Acta 1861, 1796–1807. https://doi.org/10.1016/J.BBALIP.2016.09.002.

Nauseef, W.M., Borregaard, N., 2014. Neutrophils at work. Nat. Immunol. 15, 602–611. https://doi.org/10.1038/ni.2921.

Oates, E.H., Antoniewicz, M.R., 2022. Coordinated reprogramming of metabolism and cell function in adipocytes from proliferation to differentiation. Metab. Eng. 69, 221–230. https://doi.org/10.1016/j.ymben.2021.12.005.

Okahashi, N., Kohno, S., Kitajima, S., Matsuda, F., Takahashi, C., Shimizu, H., 2015. Metabolic characterization of cultured mammalian cells by mass balance analysis, tracer labeling experiments and computer-aided simulations. J. Biosci. Bioeng. 120, 725–731. https://doi.org/10.1016/j.jbiosc.2015.04.003.

Okahashi, N., Maeda, K., Kawana, S., Iida, J., Shimizu, H., Matsuda, F., 2019. Sugar phosphate analysis with baseline separation and soft ionization by gas chromatography-negative chemical ionization-mass spectrometry improves flux estimation of bidirectional reactions in cancer cells. Metab. Eng. 51, 43–49. https://doi.org/10.1016/J.YMBEN.2018.08.011.

Okahashi, N., Matsuda, F., Yoshikawa, K., Shirai, T., Matsumoto, Y., Wada, M., Shimizu, H., 2017. Metabolic engineering of isopropyl alcohol-producing *Escherichia coli* strains with ^{13}C-metabolic flux analysis. Biotechnol. Bioeng. 114, 2782–2793. https://doi.org/10.1002/BIT.26390.

Okahashi, N., Yamada, Y., Iida, J., Matsuda, F., 2022. Isotope calculation gadgets: a series of software for isotope-tracing experiments in garuda platform. Metabolites 12, 646. https://doi.org/10.3390/METABO12070646/S1.

O'Neill, L.A.J., Kishton, R.J., Rathmell, J., 2016. A guide to immunometabolism for immunologists. Nat. Rev. Immunol. 16, 553–565. https://doi.org/10.1038/nri.2016.70.

O'Sullivan, D., vanderWindt, G.W.J., Huang, S.C.C., Curtis, J.D., Chang, C.H., Buck, M.D. L., Qiu, J., Smith, A.M., Lam, W.Y., DiPlato, L.M., Hsu, F.F., Birnbaum, M.J., Pearce, E.J., Pearce, E.L., 2014. Memory CD8$^+$ T cells use cell-intrinsic lipolysis to support the metabolic programming necessary for development. Immunity 41, 75–88. https://doi.org/10.1016/J.IMMUNI.2014.06.005.

Raam, B.J. van, Sluiter, W., Wit, E. de, Roos, D., Verhoeven, A.J., Kuijpers, T.W., 2008. Mitochondrial membrane potential in human neutrophils is maintained by complex III activity in the absence of supercomplex organisation. PLoS One 3, e2013. https://doi.org/10.1371/JOURNAL.PONE.0002013.

Remijsen, Q., Kuijpers, T.W., Wirawan, E., Lippens, S., Vandenabeele, P., Vanden Berghe, T., 2011. Dying for a cause: NETosis, mechanisms behind an antimicrobial cell death modality. Cell Death Differ. 18, 581–588. https://doi.org/10.1038/cdd.2011.1.

Riffelmacher, T., Clarke, A., Richter, F.C., Stranks, A., Pandey, S., Danielli, S., Hublitz, P., Yu, Z., Johnson, E., Schwerd, T., McCullagh, J., Uhlig, H., Jacobsen, S.E.W., Simon, A.K., 2017. Autophagy-dependent generation of free fatty acids is critical for normal neutrophil differentiation. Immunity 47, 466–480.e5. https://doi.org/10.1016/J.IMMUNI.2017.08.005.

Robinson, J.M., Karnovsky, M.L., Karnovsky, M.I., 1982. Glycogen accumulation in polymorphonuclear leukocytes, and other intracellular alterations that occur during inflammation. J. Cell Biol. 95, 933–942. https://doi.org/10.1083/JCB.95.3.933.

Rodríguez-Espinosa, O., Rojas-Espinosa, O., Moreno-Altamirano, M.M.B., López-Villegas, E.O., Sánchez-García, F.J., 2015. Metabolic requirements for neutrophil extracellular traps formation. Immunology 145, 213–224. https://doi.org/10.1111/IMM.12437.

Sadiku, P., Willson, J.A., Ryan, E.M., Sammut, D., Coelho, P., Watts, E.R., Grecian, R., Young, J.M., Bewley, M., Arienti, S., Mirchandani, A.S., Sanchez Garcia, M.A., Morrison, T., Zhang, A., Reyes, L., Griessler, T., Jheeta, P., Paterson, G.G., Graham, C.J., Thomson, J.P., Baillie, K., Thompson, A.A.R., Morgan, J.M., Acosta-Sanchez, A., Dardé, V.M., Duran, J., Guinovart, J.J., Rodriguez-Blanco, G., Von Kriegsheim, A., Meehan, R.R., Mazzone, M., Dockrell, D.H., Ghesquiere, B., Carmeliet, P., Whyte, M.K.B., Walmsley, S.R., 2021. Neutrophils fuel effective immune responses through gluconeogenesis and glycogenesis. Cell Metab. 33, 411–423.e4. https://doi.org/10.1016/J.CMET.2020.11.016.

Sake, C.L., Metcalf, A.J., Meagher, M., Di Paola, J., Neeves, K.B., Boyle, N.R., 2022. Isotopically nonstationary ^{13}C metabolic flux analysis in resting and activated human platelets. Metab. Eng. 69, 313–322. https://doi.org/10.1016/J.YMBEN.2021.12.007.

Sheikh, K., Förster, J., Nielsen, L.K., 2005. Modeling hybridoma cell metabolism using a generic genome-scale metabolic model of Mus musculus. Biotechnol. Prog. 21, 112–121. https://doi.org/10.1021/BP0498138.

Stephanopoulos, G., 1999. Metabolic fluxes and metabolic engineering. Metab. Eng. 1, 1–11. https://doi.org/10.1006/MBEN.1998.0101.

Tanner, L.B., Goglia, A.G., Wei, M.H., White, E., Toettcher, J.E., Rabinowitz, J.D., 2018. Four key steps control glycolytic flux in mammalian cells. Cell Syst 7, 49–62.e8. https://doi.org/10.1016/j.cels.2018.06.003.

Teslaa, T., Teitell, M.A., 2015. Pluripotent stem cell energy metabolism: an update. EMBO J. 34, 138–153. https://doi.org/10.15252/EMBJ.201490446.

Van Winden, W.A., Wittmann, C., Heinzle, E., Heijnen, J.J., 2002. Correcting mass isotopomer distributions for naturally occurring isotopes. Biotechnol. Bioeng. 80, 477–479. https://doi.org/10.1002/BIT.10393.

Wiechert, W., 2001. ^{13}C metabolic flux analysis. Metab. Eng. 3, 195–206. https://doi.org/10.1006/mben.2001.0187.

Winterbourn, C.C., Kettle, A.J., Hampton, M.B., 2016. Reactive Oxygen Species and Neutrophil Function, vol. 85, pp. 765–792. https://doi.org/10.1146/annurev-biochem-060815-014442.

Xu, X., Duan, S., Yi, F., Ocampo, A., Liu, G.H., Izpisua Belmonte, J.C., 2013. Mitochondrial regulation in pluripotent stem cells. Cell Metab. 18, 325–332. https://doi.org/10.1016/J.CMET.2013.06.005.

Zechner, R., Madeo, F., Kratky, D., 2017. Cytosolic Lipolysis and Lipophagy: Two Sides of the Same Coin, vol. 18, pp. 671–684. https://doi.org/10.1038/nrm.2017.76.

Zhang, J., Khvorostov, I., Hong, J.S., Oktay, Y., Vergnes, L., Nuebel, E., Wahjudi, P.N., Setoguchi, K., Wang, G., Do, A., Jung, H.J., McCaffery, J.M., Kurland, I.J., Reue, K., Lee, W.N.P., Koehler, C.M., Teitell, M.A., 2011. UCP2 regulates energy metabolism and differentiation potential of human pluripotent stem cells. EMBO J. 30, 4860–4873. https://doi.org/10.1038/EMBOJ.2011.401.